Counterflow ignition of *n*-butanol
at atmospheric and elevated pressures

Kyle Brady[†a], Xin Hui[a,b], Chih-Jen Sung[a], Kyle Niemeyer[c]

[a]Department of Mechanical Engineering
University of Connecticut
Storrs, CT 06269, U.S.A.

[b]National Key Laboratory of Science and Technology
on Aero-Engine Aero-Thermodynamics
School of Energy and Power Engineering
Beihang University
Beijing, 100191, P.R. China

[c]School of Mechanical, Industrial, and Manufacturing Engineering
Oregon State University
Corvallis, OR 97331, U.S.A.

[†]Corresponding Author:
Kyle Brady
Department of Mechanical Engineering
University of Connecticut
191 Auditorium Rd.
Storrs, CT 06269, U.S.A.
Email: kyle.brady@uconn.edu
Phone: (860)48-2492

Abstract

Critical to the development of predictive combustion models is a robust understanding of the coupled effects of chemical kinetics and convective-diffusive transport at both atmospheric and elevated pressures. The present study describes a new variable-pressure non-premixed counterflow ignition experiment designed to address the need for well-characterized reference data to validate such models under conditions sensitive to both chemical and transport processes. A comprehensive characterization of system behavior is provided to demonstrate boundary condition and ignition quality as well as adherence to the assumption of quasi-one-dimensionality, and suggest limitations and best practices for counterflow ignition experiments. This effort reveals that the counterflow ignition experiment requires special attention to ignition location in order to ensure that the assumption of quasi-one-dimensionality is valid, particularly at elevated pressures. This experimental tool is then applied to the investigation of *n*-butanol for pressures of 1–4 atm, pressure-weighted strain rates of 200–400 s^{-1}, and molar fuel loadings of 0.05–0.25. Results are simulated using two *n*-butanol models available in the literature and used to validate and assess model performance. Comparison of experimental and numerical ignition results for *n*-butanol demonstrates that while existing models largely capture the trends observed with varying pressure, strain rate, and fuel loading, the mechanisms universally over-predict experimental ignition temperatures. While several transport coefficients are found to exhibit order-of-magnitude or greater sensitivities relative to reaction rates, variation of transport parameters is not able to account for the large deviations observed between experimental and numerical results. Further comparison of ignition kernel structure and fuel breakdown pathways between mechanisms suggests that an under-prediction in the growth rate of the radical pool may be responsible for both the deviation from the experimental results and the variation in ignition temperature results observed between mechanisms.

Keywords: Counterflow ignition, Butanol, Non-premixed, Skeletal mechanism

1 Introduction

As the impacts of fossil fuel usage on energy security, climate, and human health become increasingly tangible, the need for near- and intermediate-term alternative transportation energy solutions has been recognized as a national priority. Any potential alternative fuel must provide significantly improved tailpipe emissions and reduced lifecycle carbon footprint, while requiring a minimum of changes to existing supply infrastructure. While novel engine designs and alternative fuels promise to provide efficiency gains and emissions improvements, their success is predicated upon a robust understanding of the coupled effects of chemical kinetics and convective-diffusive transport, and their accurate representation in a predictive reactive-flow model under engine relevant conditions.

Chemical kinetic model development to date has relied heavily upon homogenous experimental systems such as flow reactors, jet-stirred reactors (JSRs), shock tubes, and rapid compression machines (RCMs), primarily due to their suppression of spatial dependencies, elimination of transport effects, and ability to be relatively conveniently modeled even with very large kinetic schemes [1]. As a result, such homogenous systems have undergone appreciable improvements and modifications to better facilitate computational modeling and improve the fidelity of experimental data, as recently reviewed by Dryer et al. [2] for flow reactors, Hanson and Davidson [3] for shock tubes, and Sung and Curran [4] for RCMs. However, in practical devices combustion occurs within environments that often involve significant gradients in velocity, temperature, and species concentration, necessitating the validation of combined kinetic and transport models against computationally accessible experimental data. To address this need for transport-affected validation data, a number of low-dimensional laminar flame experiments have been developed including counterflow and stagnation flames, burner-stabilized flames, and

spherically-expanding flames, which have provided insights into flame structure, ignition, propagation, and extinction. Of these, ignition and extinction provide unique opportunities to investigate both kinetics and transport due to the relatively high sensitivity of such limit phenomena to each. However, as recently pointed out by Egolfopoulos et al. [1], they have received relatively less attention for model development compared to laminar flame speeds, in part due to the computational difficulty associated with modeling limit phenomena, but also due to the higher sensitivity resulting in greater uncertainties when boundary conditions are not well-defined. This is particularly true of transport-affected, diffusive ignition experiments, where a high-temperature boundary results in significant thermal gradients across the test section, and can lead to unquantified deviations from ideal zero-dimensional behavior [1]. Nonetheless, the sensitivity of diffusive ignition experiments – particularly non-premixed configurations – to both chemical kinetics and transport phenomena make non-premixed ignition studies an attractive and stringent option for complete model validation.

Several works have used the counterflow ignition configuration to characterize ignition properties of gaseous and liquid fuels. Fotache et al. [5] developed and used a counterflow ignition experiment to investigate the non-premixed hydrogen-air system for ambient pressures of 0.1–6 atm and characteristic strain rates of k=50–400 s^{-1}, measured locally using Laser Doppler Velocimetry (LDV). The authors experimentally verified three-limit behavior in the hydrogen-air system that had been previously observed in computational works [6,7]. Subsequent investigations by various groups in a non-premixed counterflow configuration studied a wide variety of fuels [8–26], and efforts have been extended to related configurations including premixed counterflow [27,28] and liquid-pool stagnation flows [29–32]. Of note in the aforementioned works is that large variations in the level of description of the experimental

3

apparatus and experimental procedure exist amongst the various systems and researchers. As an example of good practice, Fotache et al. [5] provided a quite detailed validation of their experimental system and procedure, including velocity and temperature gradient information along with details of their radiation correction methodology for thermocouple measurements. Reliance upon assumptions about flow quality, and presuming *a priori* quasi-one-dimensionality, can lead to crucial deviations from expected system behavior and thus it is important for any experimental system to provide a detailed characterization to demonstrate the underlying flow quality or boundary conditions. Without providing such characterization results, the application of counterflow ignition data to model development and validation is significantly hampered.

With the preceding discussion in mind, the aim of the following work is to progress three objectives. First, a new non-premixed, elevated-pressure, counterflow ignition experiment is developed and comprehensively validated in an effort to address concerns such as those mentioned previously, as well as to provide a detailed system characterization to afford a complete understanding of the system behavior and suggest "best practices" for future studies utilizing this configuration. Limitations and suggestions for improvements of the experimental system are also discussed. Second, this system is applied to the investigation of *n*-butanol, an alternative fuel with several potential advantages for applications as a fuel-additive or fossil-fuel replacement. Butanol isomers have received significant research attention in recent years, and numerous fundamental studies have been conducted using a variety of experimental systems [e.g., 33–48]. However, despite the research attention butanol isomers have garnered there is relatively little data exploring limit phenomena for these fuels. In fact, to the authors' knowledge, the only available counterflow ignition data came from the stagnation-pool study of Liu et al. [31] for *n*- and *iso*-butanol, while flame extinction data are limited to the *n*-butanol studies of Veloo et al.

[49] and Hashimoto et al. [50], and the *n-*, *iso-*, and *sec-*butanol study of Mitsingas and Kyritsis [36]. As such, the present work explores the impact of ambient pressure, strain rate, and fuel loading on counterflow ignition temperatures of *n*-butanol. Third, experimental results are simulated using *n*-butanol models available in the literature and used to validate and assess the performance of these models.

2 Experimental and computational descriptions

2.1 Experimental apparatus

As this is the first time that data from this newly built experimental system is being reported, we describe in detail the apparatus, shown schematically in Fig. 1. Flow control is accomplished through the use of sonic nozzles for all gases, with high-pressure gauges and regulators providing a wide operational flow rate range. The air stream is synthesized by a 21%/79% O_2/N_2 mixture by mole, while the fuel stream is comprised of nitrogen-diluted *n*-butanol with fuel loading varying between 5–25% by mole. To control chamber pressure and aid in moving combustible gases out of the combustion chamber, pressurized gas is extracted from a liquid nitrogen tank and metered to diffusers in the bottom of the combustion chamber. The flow rate of liquid fuel is controlled using a precision Teledyne Isco 1000D high-pressure syringe pump, with fuel vaporization accomplished through a heated spray system. Liquid fuel flowing through a capillary tube is broken up at the injector tip by a nitrogen stream heated to near the boiling point of the liquid fuel, and angled to produce a spray cone. This spray injector is inserted into a stainless steel cylinder electrically heated to just above the boiling point of the liquid fuel to prevent surface condensation – for the current study, ~140 ˚C. The remainder of the fuel line is maintained at the same temperature as the vaporization chamber. To ensure proper vaporization, the partial pressure of the fuel is maintained well below the saturation vapor pressure, calculated

using the correlation from Yaw's Chemical Handbook [51] at the temperature/pressure conditions within the fuel line. Furthermore, the fuel partial pressure never exceeds 50% of the calculated saturation vapor pressure for all experimental conditions in an effort to ensure complete vaporization.

As shown in Fig. 1, optical accessibility is facilitated by four lateral ports enclosed by UV-grade fused-silica windows. Water-cooling is provided on the exterior of the top lid to regulate the chamber surface temperature, while chamber pressure is regulated and monitored using a needle valve and digital pressure gauge on the chamber exhaust. The counterflow burner consists of a quartz straight-tube upper section directing heated air downward against a nitrogen-diluted fuel stream emanating from a stainless steel lower section. The air and fuel streams are surrounded by concentric nitrogen co-flow to isolate the test section from the ambient atmosphere and reduce curvature of the stagnation surface. The air and fuel tubes have 19 mm inner diameters and the co-flow tubes have 28 mm inner diameters. The air and fuel streams are separated by 20 mm. Contained within each main stream is a customized flow-straightening device consisting of extreme-temperature Hastelloy-X honeycomb and nichrome mesh with 40 openings per inch, located approximately 40 mm from each tube exit. These devices provide important flow straightening and laminarization, aid in establishing symmetrical flow profiles, and sufficiently flatten the velocity profile across the tube radius. The symmetry and flow balancing accomplished by these inserts are a critical factor that determines ignition location, especially at elevated pressures. A discussion of the importance of ignition location is provided in Section 3. Heating on the oxidizer side is accomplished using an internal helical SiC heater, capable of heating the airflow to 1250–1300 K at the tube exit depending on operating conditions. In addition, an external Omegalux radiant heater surrounds the air and co-flow tubes to reduce

6

radial heat loss. Both heaters are manually controlled using independent variable transformers to maintain constant power. The fuel tube surface temperature is controlled automatically using a flexible rope heater and temperature controller, while the gas temperature is monitored continuously by an in-line bare-wire K-type thermocouple located 50 mm from the tube exit.

To fully describe the ignition state in the counterflow system, the oxidizer exit temperature must be known. Since the oxidizer side is heated to typical values of 1000–1250 K to ignite the fuels of current interest, special care must be taken to accurately describe this temperature. While thermocouples are able to measure such elevated air temperatures, they can be quickly destroyed by the flame that evolves post-ignition. A customized thermocouple mount consisting of a thermocouple holder, 90-degree rotary solenoid, and motorized translation stages is used, which provides the capability for two-axis motion. To avoid flame-related damage to the thermocouple, the thermocouple holder that serves as a mounting point for an Omega Engineering K-type bare-wire thermocouple – with a wire diameter of 0.125 mm (0.005 in) – is attached to a rotary solenoid that is electrically activated from outside the combustion chamber. The solenoid is itself attached to a two-axis motorized translation stage that facilitates motion in the axial and radial directions, providing for the detailed temperature characterization discussed in Section 3.2. In addition, the thermocouple itself is subject to radiative heat transfer under high temperature conditions, necessitating a correction model to maintain fidelity of the measured thermocouple value to the actual gas temperature. The impact of radiative heat transfer is discussed in detail in the Supplementary Material.

Also required to accurately determine counterflow ignition temperatures is knowledge of the location of the ignition event. Humer et al. [21] recognized the need to determine the ignition location to ensure that ignition occurs near the experimental centerline, consistent with quasi-

7

one-dimensional assumptions. Though only atmospheric pressure experiments were conducted in [21], determination of the ignition location becomes critically important at elevated pressures, where buoyancy may cause the edges of the stagnation plane to come in close proximity to the air duct and cause ignition to occur on or near the duct rim at a different boundary air temperature than would otherwise be the case. This issue is discussed in more detail in Section 3. To facilitate this imaging, a Vision Research Phantom v710 high-speed camera is used to acquire visible-light images of the ignition event at a frame rate of 3000 Hz. This frame rate is sufficient to capture the onset of ignition, and facilitates determining its precise location within the test section. During normal operation, the camera is located at one position relative to the combustion chamber. However, during the burner alignment process the camera views the ignition event from two perpendicular angles to locate ignition in three dimensions.

2.2 Experimental procedure

In the present experiments, the oxidizer boundary temperature at the onset of ignition is denoted as the ignition temperature (T_{ig}). The procedure for acquiring this temperature is as follows: 1) The internal, external, and flow system heaters are brought up to a steady-state temperature close to the ignition state, the desired gaseous mass flow rates (excepting any fuel) for a given strain rate condition are set on the flow system, and the chamber is pressurized to the desired setpoint. 2) Fuel is introduced through the flow system and allowed to come to steady state. 3) The high-speed camera begins acquiring data, and the air temperature is gradually raised by increasing power to the internal heater until a flame ignites. 4) The fuel supply is shut off to extinguish the flame. 5) The thermocouple solenoid is activated, rotating the thermocouple bead to the center of the air duct and the air temperature, along with the fuel-side gas temperature, is recorded. 6) The images acquired from the high-speed camera are checked to verify that ignition occurs at or near

8

the longitudinal axis, and that it occurs near the middle of the test section, ±2 mm. If ignition

occurs too far towards the fuel or oxidizer exits, the flow rates are adjusted to move the

stagnation plane in the appropriate direction while maintaining a constant global strain rate (to be

defined in Section 2.3). Steps 2–6 are repeated a minimum of three times to ensure a consistent

value for T_{ig}.

2.3 Definition of characteristic strain rate

As has been discussed previously by Fotache et al. [5], defining a characteristic strain rate for the

counterflow ignition configuration that exhibits a clear, monotonic relationship with ignition

temperature can prove somewhat troublesome. Two general options were described in [5]: the

strain rate may be defined by a measured velocity gradient (i.e., local strain rate) or by the

boundary conditions (i.e., global strain rate). As laid out by Fotache et al. [5], the ideal definition

would describe the strain rate at the precise axial location where ignition occurs. However, this

local definition requires prior knowledge of its location. An alternative local strain definition was

adopted by Fotache et al. [5] in the form of the maximum measured strain rate on the oxidizer

side, which was shown to behave similarly to the kernel-based definition due to its description of

the strain rate in the vicinity of the kernel. The choice of the oxidizer side is the result of their

observation that ignition occurs on this side due to its exponential dependence on temperature

compared to a linear dependence on fuel concentration. However, for the current apparatus, the

solid seeding particles necessary to perform velocimetry in high-temperature flows would

quickly clog the oxidizer-side mesh insert described in Section 2.1. A similar local definition

could be applied on the fuel side of the stagnation plane, where cooler temperatures allow the use

of liquid seeding particles, similar to Liu et al. [19]. However, the fuel-side strain rate does not

maintain a constant relationship with the oxidizer-side strain rate as temperature − and thus

9

density – of the oxidizer stream changes. As can be readily demonstrated computationally by keeping total mass flux constant for each stream, as the oxidizer boundary temperature varies, the resultant strain rate near the stagnation plane on the oxidizer side also varies, whereas the fuel-side strain rates are indistinguishable. Since counterflow ignition inherently involves variation of the oxidizer temperature, this behavior suggests that the fuel-side strain rate is not an appropriate strain rate definition for counterflow ignition.

Alternatively, the strain rate near the ignition kernel may be estimated from the boundary conditions. Such a global definition, while simple to apply, invokes assumptions regarding the nature of the boundary conditions, which may or may not accurately describe those observed experimentally. As such, it is critical to understand the nature of the velocity boundary conditions in order to select an appropriate flow model, namely potential flow or plug flow. A comparison of axial velocities measured by Particle Image Velocimetry (PIV) along the stagnation streamline to the commensurate potential- and plug-flow models is provided in Fig. 2. For atmospheric pressure and room temperature boundaries, it is immediately apparent that the measured profile does not exactly match either flow model, but instead represents an intermediate between the two. While this result is not unexpected for a practical counterflow device [52], it is seen from Fig. 2 that the plug flow model clearly better matches the measured velocity profiles near the boundaries.

In addition to choosing the correct flow model, it is imperative to capture the effects of varying density due to the large temperature gradients inherent to counterflow ignition. This can be accomplished using the relations of Seshadri and Williams [53]:

$$k = \frac{2V_O}{L}\left(1 + \frac{V_F\sqrt{\rho_F}}{V_O\sqrt{\rho_O}}\right),$$ Eqn. 1

where k is the strain rate, V is the bulk velocity at the boundary, L is the separation distance, ρ is the density, and the subscripts F and O represent the fuel and oxidizer boundaries, respectively. It is worth noting that the strain rate calculated from Eqn. 1 refers to the estimated characteristic strain rate on the oxidizer side of the stagnation plane. For the case in Fig. 2, the measured maximum strain rate is 126 s^{-1} as compared to an estimated 150 s^{-1} using Eqn. 1, demonstrating the adequacy of this global strain rate definition.

Finally, as is noted in the work of Kreutz and Law [7], the width of the mixing layer in the counterflow arrangement scales as a function of $(\rho k)^{-1/2}$, such that for constant strain rate, ambient pressure/density changes will result in appreciable variations in the relevant spatial scales. Thus, in order to isolate the chemical effect of pressure variations from the effect of varied spatial structure, the anatomy of the flow field (in terms of temperature and concentration profiles) is kept approximately constant through the use of the pressure-weighted strain rate (k'), as first used experimentally in the work of Fotache et al. [5] and defined in Eqn. 2:

$$k' = \frac{P_C}{P_{ref}} k, \qquad\qquad \text{Eqn. 2}$$

where P_C is the chamber pressure, P_{ref} is a reference pressure, taken throughout this work as 1 atm, and k is the oxidizer-side global strain rate as defined in Eqn. 1. Thus, when the pressure-weighted strain rate is held constant the width of the pre-ignition mixing layer is expected to be approximately invariant with pressure. By measuring temperature and velocity as functions of position within the test region, this invariance is borne out experimentally in Section 3.

2.4 Computational specifications

In order to assess the fidelity of existing combustion models to experimentally-derived counterflow ignition temperatures for *n*-butanol, the ignition state is modeled based on the work of Kreutz et al. [6], with the ignition temperature corresponding to the turning point of the lower-branch ignition response curve with respect to oxidizer boundary temperature. The formulation of the counterflow non-premixed configuration follows that of Smooke et al. [54], while the navigation of the ignition turning point is achieved using the flame-controlling continuation method developed by Nishioka et al. [55]. In this study the controlled species is chosen as the H radical due to its physical significance to ignition, although, as shown by Kreutz and Law [7], ignition response curves could be generated using other key radical species as well.

It is important to recognize that the flow description used in Smooke et al. [54] is potential flow, while experimentally the strain rate is described by a plug-flow global formulation. Despite the varying description of the velocity boundary conditions, as demonstrated by Sung et al. [56], the scalar structures of different flow descriptions – potential, plug, or an intermediate flow – collapse onto each other within the thermal mixing zone. Fotache et al. [8] further indicated the insensitivity of the ignition process to the flow model used. As a result, the choice of flow model should have a minimal effect on the ignition temperatures computed.

A number of detailed kinetic mechanisms for butanol isomers have been developed in recent years, including the mechanisms of Frassoldati et al. [45], Merchant et al. [46], and Sarathy et al. [48], hereafter referred to as the Frassoldati mechanism, Merchant mechanism, and Sarathy mechanism, respectively. The Frassoldati mechanism, which is an update of the mechanism of Grana et al. [39], includes all four isomers and was validated primarily against low-pressure flame speciation data. The Merchant mechanism, which includes all four isomers and was based

upon the comprehensive mechanism of Van Geem et al. [47], was validated against pyrolysis, flame speed, low-pressure flame structure, and shock tube data. The Sarathy mechanism was validated against flame speeds, low-pressure flame structure data, RCM and shock tube ignition delays, and JSR species profiles. Unfortunately, the inclusion of non-integer stoichiometric coefficients in the Frassoldati mechanism makes it incompatible with the current Chemkin-based ignition code. Hence, only the Sarathy and Merchant mechanisms are included and compared in the present study.

An important limitation in the current study – and indeed in combustion modeling in general – is the size of the chemical kinetic model and its accompanying computational cost. While the sizes of the Sarathy (426 species, 2335 reactions) and Merchant (372 species, 8723 reactions) mechanisms are modest compared to many mechanisms for fuels of practical interest, they are nonetheless prohibitively large for use in computing ignition turning points. As a result, skeletal mechanisms specific to *n*-butanol are created using the Directed Relation Graph with Error Propagation (DRGEP) implementation of the Mechanism Automatic Reduction Software (MARS) package of Niemeyer and co-authors [57–60]. Each mechanism is reduced using constant-volume ignition delays for equivalence ratios of 0.5–2, pressures of 1–40 atm, and temperatures of 1000–1800 K, using the fuel, N_2, and O_2 as target species. In addition, the reduction procedure utilizes perfectly stirred reactor (PSR) extinction profiles for inlet temperatures of 400 and 500 K, covering the same range of pressure and equivalence ratio as the autoignition results.

With an error limit of 10% (defined in terms of autoignition delay and PSR extinction turning point), the final skeletal mechanism for the Sarathy mechanism consists of 120 species and 832 reactions, while that for the Merchant mechanism consists of 102 species and 1904

reactions. The skeletal mechanisms generated were validated against their corresponding detailed mechanisms using ignition delays, PSR temperature response curves and extinction turning points, and laminar flame speeds – all showing good agreement within the specified error limit. Sample validation results are included in the Supplementary Material.

While the Merchant and Sarathy skeletal mechanisms have been validated under both homogenous and flame conditions, it is important to ensure that they also adequately follow the behavior of the detailed mechanisms for the conditions in this study. To that end, Fig. 3 demonstrates the degree of matching between the predicted ignition turning points for the skeletal and detailed mechanisms at 1 and 5 atm conditions. At both pressures, the skeletal Sarathy mechanism results differ negligibly from those of the detailed mechanism, with a maximum difference in the predicted turning point temperature of 2 K at the 5 atm pressure. The skeletal Merchant mechanism exhibits a larger difference of 4 K at 1 atm and 14 K at 5 atm, however this difference, 0.3–1% of ignition temperature, is deemed small in a relative sense.

2.5 Mixing zone and ignition kernel structure

To provide a basis for understanding the behavior of the counterflow ignition system, Fig. 4 demonstrates typical spatial profiles at the ignition turning point for velocity, temperature, and the mole fractions of n-butanol, oxygen, and H, O, OH, and HO_2 radicals, computed using the skeletal Sarathy mechanism. Several important features are evident. First, the "ignition kernel" – taken throughout this work to refer to the localized region of maximum H, O, OH, and HO_2 radical mole fractions – is located on the oxidizer side of the stagnation plane at a region with temperatures very near that of the oxidizer boundary. This position is the result of the high activation energies of the chain branching reactions that are primarily responsible for production of these radicals. Since the rate of radical production is exponentially dependent on temperature

14

and linearly related to fuel concentration, the ignition kernel is located on the oxidizer side for all conditions in the present study. Second, the fuel transports towards the oxidizer side and the radicals generated within the ignition kernel must be transported across the stagnation plane to react with fuel. This spatial separation results in a fuel-lean condition at the ignition kernel, and is responsible for the counterflow ignition experiment's relatively high sensitivity to transport properties. Third, thermal mixing between the hot oxidizer and cold fuel streams occurs over nearly the same region as fuel/oxidizer mixing and encompasses the ignition kernel. This zone taken as a whole is referred to as the thermal mixing zone throughout the following study.

3   Experimental validation

As mentioned in Section 1, the first goal of the present study is to provide a comprehensive characterization of the newly developed counterflow ignition apparatus, both to ensure reasonable adherence to quasi-one-dimensional assumptions made in the numerical model and to better aid in comparison amongst other similar experimental systems. To this end, the following sections describe a detailed characterization at atmospheric and elevated pressures.

3.1 Velocity

While a global estimate is used to describe strain rate in the current work, the counterflow ignition experiment has been rigorously examined using PIV to observe the nature of the flow field as functions of strain rate, pressure, and – to a limited extent – temperature variations. The counterflow velocity field is obtained by cross-correlating time-delayed image pairs obtained from a Dantec Dynamics digital PIV system. The interrogation sub-region size was set at 32×32 pixels with 50 percent overlap. Pulse delays were set to follow the "¼ rule" such that the average inter-frame particle movement near the region of interest did not exceed one quarter of the sub-region size. Particle seeding is accomplished using an Oxford Lasers 10Bar MicroSeeder, which

is capable of operating at elevated pressures and provides 50 cSt silicone oil droplets with sizes ranging from 0.5–5 µm. It is worth noting that, since the boiling point of the silicone oil is ~570 K, it is not possible using the current setup to obtain velocity fields at typical operating temperatures. While solid particles could overcome this problem, this is not feasible in the current setup as described in Section 2.3. Despite this limitation, the salient issues of quasi-one-dimensionality, velocity boundary conditions, and the impact of pressure variations may still be explored at temperatures below the seed fluid boiling point.

To begin to address the issue of quasi-one-dimensionality in the flow field, it is most informative to observe the axial velocities measured across the diameter of the top and bottom ducts. Figure 5 shows the axial velocity at each duct exit as a function of radial distance under 1 and 3 atm with a pressure-weighted global strain $k' = 150$ s^{-1}. At both atmospheric and elevated pressure, a large and nearly flat core region representing approximately 60% of the tube diameter exists near the experimental centerline. It is also apparent from Fig. 5 that the fuel and oxidizer velocity profiles are reasonably well balanced at varying pressures, as the extent of the core regions for both streams is quite comparable. One feature of note on the oxidizer side is the presence of a small velocity deficit near the central axis. This deficit is due to the internal heater in the oxidizer flow, which terminates just upstream of the flow-straightening mesh. However, at elevated temperatures, as demonstrated in Fig. 6, the effect of heat addition along the centerline by the internal heater cancels the effect of this velocity deficit, and results in an improved – and rather flatter, albeit slightly smaller – core region.

In addition to radial profiles, the axial velocity along the experimental centerline is valuable not only for its ability to determine correspondence to a given flow model (*cf.* Fig. 2), but it also facilitates a validation of the pressure-weighted strain rate concept. Figure 7 shows the results at

16

unheated conditions, for pressures of 1 and 3 atm and $k' = 150 \text{ s}^{-1}$. While the absolute magnitude

of the 1 and 3 atm axial velocity profiles are quite different, when the 3 atm results are weighted

to account for the density difference by a method similar to Eqn. 2, the spatial structure of the

pressure-weighted velocity profile corresponds well to the measurements at 1 atm. Hence, Fig. 7

demonstrates that comparison across pressures at a given pressure-weighted strain weight is in

fact valid.

3.2 Temperature

It is also critical to the fidelity of the ignition data to ensure quasi-one-dimensional behavior with

respect to temperature in addition to the velocity validation demonstrated in the previous section.

This may be accomplished by observing the temperature field within the test section as a

function of radial and axial position. Figure 8 shows the radial temperature profiles at the

oxidizer duct exit − not corrected for radiative losses − for a pressure-weighted strain rate $k' =$

300 s^{-1} at 1 and 3 atm chamber pressures. At both 1 and 3 atm, the symmetry of the temperature

profile is maintained, as is the overall shape and size of the radial profile at several axial

locations. In addition, a core region with only limited temperature gradient in the radial direction

can be observed in the range of ±5 mm from the centerline for each pressure condition.

    Figure 9 further demonstrates the axial temperature profiles by keeping heater power

constant while varying the stagnation plane location through the changes in oxidizer duct mass

flow rate, for a pressure-weighted strain rate $k' = 300 \text{ s}^{-1}$ at chamber pressures of 1 and 3 atm.

Two critical features of the counterflow arrangement are validated in Fig. 9. First, the three 1 atm

cases clearly show that the location of the stagnation plane does not impact the overall structure

of the thermal mixing zone. This feature is important as it clearly demonstrates that the mixing

zone is unaffected by changes in the stagnation plane location so long as it is not excessively

close to either boundary. Second, this structure is maintained when the chamber pressure is raised to 3 atm, with the width and temperature gradient being nearly identical to that of 1 atm, as is more clearly demonstrated with position-shifted temperature profiles in the inset to Fig. 9 by collating the thermal mixing zone. Therefore, the inset of Fig. 9 shows that the thermal structure similarity of the test section is maintained at constant pressure-weighted strain rate.

3.3 Fuel concentration

To fully characterize the boundary conditions of the counterflow system, the concentrations of reactants must be known. For liquid fuel such as *n*-butanol, it must first be completely vaporized and mixed with its nitrogen diluent, and then must remain vaporized as it travels to the combustion chamber. This necessitates elevated temperatures along the entirety of the fuel line in order to avoid condensation; however, excessive temperature may foster premature fuel breakdown such that the composition on the fuel side consists of diluted fuel and fuel fragments. Thus a balance must be struck between the juxtaposed needs of ensuring complete vaporization and preventing fuel decomposition in order to establish an accurate description of the fuel stream concentration boundary condition.

To ensure that no condensation or decomposition occurs at local cold or hot spots, a gas chromatograph/mass spectrometer (GC/MS), Shimadzu GC-QP2010S, is employed to allow for simultaneous identification and quantification of species present within a gas sample. Typical *n*-butanol GC/MS results are shown in Fig. 10. A single *n*-butanol peak is observed, with nitrogen eluting prior to the detector start time. No secondary peaks are observed within the measured baseline, as demonstrated through magnification of the baseline in the left inset to Fig. 10. The lack of additional peaks prior to *n*-butanol indicates that no measurable fuel decomposition occurs within the fuel stream prior to the combustion chamber.

In addition to demonstrating adequacy with respect to fuel breakdown, it is also necessary to show that the concentration matches the expected value based upon the flow rate of the fuel pump. This can be readily evaluated via the *n*-butanol peak areas. The right inset of Fig. 10 shows peak areas from successive samples of *n*-butanol/nitrogen from the fuel stream. As is visually apparent, such runs are highly consistent in terms retention time, peak shape, and total area. Using a pooled standard deviation of samples taken from multiple sample bottles, the resulting standard deviation in peak area is calculated as 1.57% of the mean, indicating a high degree of repeatability across all samples, with the mean sample concentration falling within 11% of expected values based on flow settings. Given that typically-quoted values of estimated uncertainty lie between 7–15% for similar GC/MS analyses [61–63], this level of matching between predicted and measured fuel loading, combined with the degree of observed repeatability in ignition results, suggests that the predicted fuel mole fractions are in fact representative of the real boundary conditions.

3.4 Ignition location

The preceding discussions of velocity, temperature, and concentration validations have focused on understanding the steady-state behavior of the counterflow ignition apparatus, and ensuring that the system behaves – to within a reasonable approximation – quasi-one-dimensionally. However, ignition is inherently a transient process; the fidelity of any experimental data hinges on the assumption that ignition itself behaves in a quasi-one-dimensional manner. This does not happen automatically. Even for a flow field with no obvious defects in boundary conditions, ignition may still occur at unexpected locations for any of a variety of reasons, including insufficient or uneven shroud flow, local velocity imbalances, and small (almost imperceptible via flame observation or PIV measurements) duct misalignments.

19

Figure 11 demonstrates an out-of-bounds ignition event for $k' = 350$ s^{-1}, *n*-butanol mole fraction in the fuel stream $X_f = 0.15$, and P = 4 atm. At t = 0 ms, a flame becomes just visible in the top-left corner of the frame, and proceeds to propagate along the mixing layer between the air and fuel streams until it reaches a nearly steady-state form ~23 ms later. It is readily apparent from this progression that the onset of ignition occurs far away from the well-characterized core-region, at a location where the relationship between the oxidizer boundary conditions and the ignition kernel conditions is unclear. In addition, this process occurs quickly enough that it is not possible to observe in the absence of high-speed imaging. Thus, without a method of determining ignition location, it is not possible to ascertain whether ignition has occurred prematurely due to an ignitable state being reached in the outer regions of the flow field before an ignitable state was reached within the core region. This can result in several problems when collecting ignition data, including an underestimation of ignition temperatures or an inability to repeat previously collected data sets. It is important to note that this problem is most critical when attempting to collect ignition data at elevated pressures. Since the effects of buoyancy become more prevalent as pressure increases, the "wings" of the stagnation plane move closer to the co-flow tube wall, resulting in an increased likelihood of hot surface ignition. It is for this reason that the upper limit for ignition data derived from the current system is set at 4 atm; within this pressure limit ignition has been found to reliably occur within the core region.

Typical ignition sequences for pressures of 1 and 3 atm are shown in Fig. 12. In contrast to Fig. 11, ignition in Fig. 12 occurs along the centerline of the experiment, well within the core region and centered between the fuel and air boundaries. Once initiated at t = 0 ms, the flame propagates outwards in a largely symmetrical manner and reaches its steady-state form in

approximately 9 ms. The consistent ignition location instills an additional degree of confidence for the reported datasets.

3.5 Ethylene ignition temperature comparison

For the purposes of providing a comparison between the results of the current experimental system and those derived from other similar systems, a comparison of ethylene ignition temperatures at atmospheric pressure and fuel loading $X_f = 0.15$ is provided in Fig. 13 based on the data of Humer et al. [21]. This dataset is chosen as a basis for comparison since it is directly comparable due to the authors' identical global strain rate definition. To provide a more complete comparison, and to demonstrate the effect of differing radiation correction models, two corrected ignition temperature results are presented. The first represents the radiation correction used for all subsequent data derived from this system, which is described in detail in the Supplementary Material. The second correction method is similar to the procedure of Humer et al. [21], the salient feature of which is the assumption of a constant Nusselt number about the thermocouple bead Nu = 2. As is readily observed, for similar radiation correction procedures the present data very closely follows the trend observed by Humer et al. [21] and falls within 30–40 K of the absolute value across the strain rate range. While the source of the discrepancy between the two Nu = 2 datasets is not known, one possible cause is differing thermocouple designs and support structure, as is described in the Supplementary Material. When a variable Nusselt number formulation based on the bulk velocity is used (*cf.* Supplementary Material), the magnitude of the radiation correction is larger and the resulting ignition temperature results are closer to the data reported by Humer et al. [21]. Hence, Fig. 13 demonstrates that the choice of radiation correction methodology can also be important.

21

4   Ignition results and discussion

4.1 Effects of aerodynamic strain rate

Figure 14 demonstrates the impact of varied strain rate on the experimentally-derived ignition temperature of *n*-butanol, as well as the results of the numerical simulations using skeletal mechanisms derived from the butanol mechanisms of Sarathy et al. [48] and Merchant et al. [46] for the same imposed conditions. For 1 and 3 atm ambient pressures, $X_f = 0.15$, and $k' = 200$–400 s^{-1}, the ignition temperature increases monotonically by ~20 K, at essentially the same rate regardless of the ambient pressure. However, the increase in pressure does result in a downward shift in ignition temperature by approximately 100 K. Similar strain rate effects have been observed previously by Fotache et al. [8,9] for short-chain alkanes and is attributable to the thinning of the ignition kernel width and commensurate reduction in characteristic residence times associated with increasing strain rate, resulting in increased convective/diffusive losses of heat and radicals. Turning to the numerical results, the Sarathy and Merchant mechanisms produce nearly identical trends, very slightly over-predicting the experimental rate-of-change of ignition temperature with increasing strain rate. It is worth noting that a similar over-prediction of the effect of strain rate was observed by Liu et al. [31] using a previous version of the Sarathy mechanism [35] in their liquid-pool stagnation study, where strain rate was defined locally via LDV measurements. This consistent over-prediction despite varied strain rate definitions suggests that the discrepancy is unlikely to be due to how the strain rate is characterized. It is further noted that the primary discrepancy between the experimental and numerical results is an upward shift of 80–100 K for the Sarathy mechanism and 130–160 K for the Merchant mechanism. In absolute terms this deviation of ~7–14% is comparable to the effect of changing the fuel loading from $X_f = 0.05$ to 0.25 (*cf.* Section 4.2) or ambient pressure from 1 to 4 atm (*cf.*

22

Section 4.3). Thus, this degree of discrepancy is consistent across all conditions investigated and should be considered significant within the context of the experimental results.

4.2 Effects of fuel loading

Figure 15 demonstrates the effects of varied fuel loading for $X_f = 0.1$–0.25 for 1 atm and $X_f = 0.05$–0.2 for 3 atm, by keeping k' constant at 300 s^{-1}. As is most clear from the 3 atm results, at very low fuel concentrations the ignition temperature is significantly affected by small changes in fuel concentration, while at higher concentrations the ignition temperature becomes progressively less sensitive to increases in fuel concentration at the fuel boundary. Because of constant k', the characteristic mixing zone thickness remains similar when varying X_f. As fuel loading increases, the effective fuel flux to the ignition kernel increases, resulting in lower ignition temperatures. In addition, the ignition temperature begins to plateau as fuel loading surpasses $X_f = 0.2$–0.25, showing that the effective fuel flux becomes progressively less limiting to ignition. The observed "plateau" is similar to the behavior observed by Fotache et al. for C_1–C_4 alkanes [8,9] and Liu et al. for C_3–C_{12} alkanes [19]. Furthermore, as is the case for strain rate variations, both the Sarathy and Merchant mechanisms capture the experimentally observed trend with increasing fuel concentration, but the results are uniformly shifted upward by ~100 K for the Sarathy mechanism, and ~140–160 K for the Merchant mechanism.

4.3 Effects of pressure

The impact of elevated pressure in the range of 1–4 atm is shown in Fig. 16 for $X_f = 0.15$ and $k' = 350$ s^{-1}. As pressure is increased at constant fuel loading and pressure-weighted strain rate, ignition temperature monotonically decreases, dropping by ~120 K over the pressure range. This indicates enhanced reactivity with increasing pressure. While the mechanism predictions are shifted upward to a similar extent as seen in Figs. 14 and 15, the ignition temperature trend is

largely captured by both mechanisms, with the Merchant mechanism slightly over-predicting the pressure sensitivity.

To begin to explore the important chemistry and transport controlling n-butanol's pressure behavior, sensitivity analyses are conducted for reaction rates (by perturbing pre-exponential factors, A_i's) and binary diffusion coefficients (by perturbing the zeroth-order coefficients of the polynomial fits for D_{jk}'s) defined as $S_{Ai} = \frac{\partial ln T_{ig}}{\partial ln A_i}$ and $S_{Djk} = \frac{\partial ln T_{ig}}{\partial ln D_{jk}}$, respectively. As such, sensitivity coefficients with positive signs suggest that ignition temperature increases with an increase in reaction/diffusion rates, while a negative result suggests a decrease in T_{ig} (i.e., promoting ignition). Results of such an analysis are shown in Fig. 17 for the ten reactions and diffusion pairs of greatest magnitude at $k' = 350$ s^{-1}, $X_f = 0.15$, and pressures of 1 and 4 atm. The results from the Sarathy mechanism are shown in Figs. 17 (a)-(c), while those obtained utilizing the Merchant mechanism are demonstrated in Figs. 17 (d)-(f). It is seen from Fig. 17 that both mechanisms yield highly similar sensitivity results. For the purposes of clarity in exploring the ignition temperature's pressure-dependency, the following discussion will focus on the results from the Sarathy mechanism except where explicitly noted. A discussion of the differences between the Sarathy and Merchant mechanisms for non-premixed ignition follows in Section 4.4.

A general observation immediately apparent upon inspection of Fig. 17 is the dominant effect of transport properties on the ignition temperature. Comparing the axes of Figs. 17 (a) and (b)/(c), it is clear that the nitrogen-fuel diffusivity exhibits sensitivities almost two orders of magnitude larger than that of the most sensitive chain branching reactions in Fig. 17 (b) or (c). As has been observed previously in similar systems [19,30], the non-premixed structure of the mixing zone results in very large sensitivities of the fuel-air binary diffusivities due to the necessity for fuel to diffuse across the stagnation plane to the ignition kernel. Thus, an

24

enhancement of the binary diffusion rates of fuel with nitrogen and oxygen will tend to promote ignition. In addition to the intuitive importance of fuel transport, the binary diffusion rates of several intermediate products exhibit equal or greater ignition sensitivities compared to the most sensitive reaction rates. As the peak mole fractions of these intermediates are offset towards the fuel side from the peak concentrations of the O, OH, and H radicals, the ability for intermediates to diffuse towards the ignition kernel plays an important role in the diffusive ignition systems.

Also of interest in Fig. 17(a) is the significant change in the sensitivity of hydrogen peroxide transport at elevated pressure. Whereas at atmospheric conditions ignition is minimally affected by its diffusion rates, at 4 atm ignition temperature is predicted to be 3 times more sensitive to nitrogen-hydrogen peroxide diffusion rates than the rate of chain branching reactions. This difference is attributed to the significant changes in the fuel chemistry over this pressure range. While the chain-branching reaction R1 exhibits the largest negative sensitivity at atmospheric pressure (*cf.* Fig. 17 (c)), ignition becomes primarily sensitive to hydrogen peroxide scission (R2) at 4 atm, as shown in Fig. 17 (b).

$$H + O_2 \rightarrow O + OH \hspace{4cm} \text{R1}$$

$$H_2O_2(+M) \rightarrow 2OH(+M) \hspace{3.5cm} \text{R2}$$

This transition in chain branching mechanism mirrors that of the hydrogen ignition limits [5], where the system transitions between the second limit (with chain branching dominated by R1) and the third limit (typified by reactions involving hydroperoxyl and hydrogen peroxide, e.g., R2) at pressures of 3–4 atm. Since R2 is a high activation energy reaction, and the peak hydrogen peroxide mole fraction is shifted towards the cooler fuel side of the ignition kernel (*cf.* Fig. 18), enhanced diffusion of hydrogen peroxide would promote its losses to a low-temperature region where this reaction would not be favored and thus inhibit ignition (positive sensitivity).

Further inspection of Fig. 17 highlights several other interesting features within the *n*-butanol chemistry. First, when sorted by the sensitivity magnitude at 4 atm (Fig. 17 (b)) it is apparent that destruction of the parent fuel by hydroperoxyl plays an appreciably more prominent role at elevated pressure than atmospheric pressure. A flux analysis comparison between these two conditions reveals that the reaction R3:

$$n\mathrm{C_4H_9OH} + \mathrm{HO_2} \rightarrow \alpha\,\mathrm{C_4H_8OH} + \mathrm{H_2O_2} \qquad\qquad \text{R3}$$
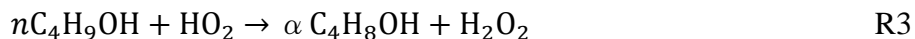
accounts for ~10.4% of fuel consumption at 4 atm, and only 3.6% at 1 atm. Similar behavior is observed from the Merchant mechanism, albeit for H-abstraction from the β-site (*cf.* Fig. 17 (e)). In addition, taken together R2 and R3 are chain-branching and grow the radical pool at 4 atm. Under atmospheric conditions R2 is relatively inactive and hydrogen peroxide serves primarily as a radical sink.

Second, when sorted by the sensitivity magnitude at 1 atm (Fig. 17 (c)), several of the more sensitive reactions involve the formyl radical:

$$\mathrm{C_2H_4} + \mathrm{O} \rightarrow \mathrm{CH_3} + \mathrm{HCO} \qquad\qquad \text{R4}$$

$$\mathrm{HCO} + \mathrm{O_2} \rightarrow \mathrm{CO} + \mathrm{HO_2} \qquad\qquad \text{R5}$$

$$\mathrm{HCO} + \mathrm{M} \rightarrow \mathrm{H} + \mathrm{CO} + \mathrm{M}, \qquad\qquad \text{R6}$$
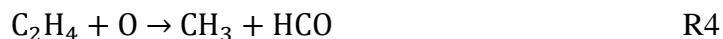
which are minimally important at 4 atm. Again, similar results are obtained from the Merchant mechanism, with the exception of R4, which does not appear in the present sensitivity analysis shown in Fig. 17 (f). The underlying causes of both of the above features are evident in Fig. 18, which compares the spatial profiles of important radical species and hydrogen peroxide at 1 and 4 atm corresponding to the open circles in the Sarathy mechanism results in Fig. 16 (T_{ig} = 1310 and 1173 K, respectively). While the peak mole fractions of H, O, OH, and formyl radicals are lower at 4 atm than 1 atm by an order of magnitude or more, hydroperoxyl mole fractions remain

relatively constant, and hydrogen peroxide mole fractions increase with pressure. As a result, the relative importance of reactions R2 and R3 is enhanced at elevated pressure. Conversely, appreciably less formyl radical is present in the ignition kernel at 4 atm, and path flux analysis reveals that additional carbon monoxide formation pathways involving the ethynyloxy and vinyloxy radicals become important at elevated pressures, thus reducing the importance of formyl to the reduction of fuel intermediates to carbon monoxide.

4.4 Sources of combustion model disagreement

Observing Figs. 14, 15, and 16, two obvious trends emerge. First, both the Sarathy and Merchant mechanisms over-predict the experimental data to an appreciable extent. Second, while each mechanism predicts very similar trends, the Merchant mechanism uniformly predicts higher ignition temperatures by ~50–80 K. This raises two corresponding questions; what is the source of the discrepancies between the models and experimental data, and what is responsible for the disparity between the two models? As such, the following discussion attempts to address both of the aforementioned questions.

Recalling the sensitivity results of Fig. 17, a handful of reactions and diffusion pairs exhibit large sensitivities, suggesting they may play a predominant role in determining the ignition turning point for a given mechanism. Regarding the transport properties, it is noted that the databases employed in the two mechanisms are very similar. The effect on the ignition turning point of manually changing important transport parameters of *n*-butanol, C_2H_4, and C_2H_3OH (selected based on the sensitivity results) in the Merchant mechanism to their corresponding values in the Sarathy mechanism is first examined. For the conditions tested, modification of these transport properties cannot account for the ignition temperature difference predicted by the two mechanisms, with *n*-butanol leading to a ~5 K shift, C_2H_4 further reducing ignition

temperature by ~2 K, and C_2H_3OH increasing the turning point by ~1 K. Hence, the disparity between two mechanisms cannot be attributed to differences in the transport parameters for key diffusion pairs.

As shown in Fig. 3, while the ignition temperatures predicted by the Merchant and Sarathy mechanisms differ by 62 K at 1 atm and 43 K at 5 atm, for each pressure their peak H-radical mole fractions at the respective turning points are of similar size. In fact, the ignition kernel structure in terms of important radicals (and hydrogen peroxide) are remarkably similar when the structure at the respective ignition turning points are compared, with peak O, OH, H, and HO_2 mole fraction predictions within a factor of two of each other. Although each mechanism predicts an ignition kernel with a roughly equivalent radical pool size, the Merchant mechanism reaches this critical size more slowly (and hence exhibits higher ignition temperature) relative to the Sarathy mechanism. The likely cause of this behavior is demonstrated in Fig. 19 for P = 1 atm, $k' = 350$ s^{-1}, and $X_f = 0.15$ through a path flux analysis for the destruction of *n*-butanol. After an initial H-abstraction reaction leading to hydroxybutyl radicals, the Sarathy mechanism (Fig. 19 (a)) predicts further reactions proceeding primarily through unimolecular decomposition pathways. In contrast, the Merchant mechanism (Fig. 19 (b)) predicts that nearly half of the hydroxybutyl radicals are consumed through H-abstraction reactions to form enols or butyraldehyde. These intermediates are themselves consumed through various H-abstraction pathways, forming additional products that are primarily consumed in the same way. As a result, significantly more O, OH, and H consumption is involved in fuel breakdown in the Merchant mechanism relative to the Sarathy mechanism, and likely accounts for the slower radical pool growth and thus the overall higher predicted ignition temperatures.

Similarly, it is possible that the growth rate of the radical pool is also responsible for the disparity between experimental and numerical results. If overall slower growth of the radical pool is responsible for the large disparity between mechanisms, a similar under-prediction of radical pool growth rate could also account for the discrepancy between the models and the experimental results.

5   Conclusions

The present study progresses two objectives. First, a new variable-pressure counterflow ignition experiment is developed and comprehensively validated. This validation process aids in the comparison of experimental data to numerical model results by way of testing the experimental adherence to presumed quasi-one-dimensionality. In addition to measuring velocity, temperature, and concentration boundary conditions, ensuring that ignition occurs near the experimental centerline is critical to the validity of experimental results, particularly at elevated pressures. Furthermore, due to the necessity of identifying the location of ignition, high-speed imaging of all ignition events is an indispensible tool for counterflow ignition data.

Second, the new experimental system is used to investigate the ignition temperature trends of *n*-butanol as a function of strain rate, fuel loading, and pressure. This data is then compared to two skeletal mechanisms developed from currently available comprehensive butanol mechanisms to investigate their ability to predict experimentally observed trends. This comparison results in a number of conclusions:

- The experimental trends in terms of strain rate, fuel loading, and pressure are largely captured by both the Sarathy et al. [48] and Merchant et al. [46] mechanisms. However, both mechanisms over-predict the experimental data to an appreciable extent, with the Sarathy mechanism predicting uniformly lower temperatures compared to the Merchant mechanism.

29

- Counterflow ignition of *n*-butanol is shown to be sensitive to the transport of fuel and intermediate molecules. Normalized sensitivities of reaction rates are appreciably lower even for the most sensitive chain-branching reactions.

- The two mechanisms tested appear to largely agree on the size of the radical pool – in terms of O, OH, and H radicals – at which ignition occurs. However, the overall growth rate of the radical pool as a function of boundary temperature is much smaller in the Merchant mechanism, leading to higher ignition temperatures.

- The source of disagreement between the two butanol models is analyzed and discussed, with the Merchant mechanism predicting a significant portion of the parent fuel breaking down through enol and aldehyde pathways, as compared to primarily scission reactions in the Sarathy mechanism. The pathways considered in the Merchant mechanism deplete the radical pool and result in overall slower growth of the ignition kernel.

- The over-prediction of experimental ignition temperatures by both mechanisms is likely attributable – at least in part – to an under-prediction of the growth rate with respect to oxidizer temperature of the radical pool.

Acknowledgements

Supplementary Material

Appendix A: Thermocouple radiation correction

Appendix B: Uncertainty analysis

Appendix C: Sample model validation results

References

[1]   F.N. Egolfopoulos, N. Hansen, Y. Ju, K. Kohse-Höinghaus, C.K. Law, F. Qi, Prog. Energy Combust. Sci. 43 (2014) 36–67.

[2]   F.L. Dryer, F.M. Haas, J. Santner, T.I. Farouk, M. Chaos, Prog. Energy Combust. Sci. 44 (2014) 19–39.

[3]   R.K. Hanson, D.F. Davidson, Prog. Energy Combust. Sci. 44 (2014) 103–114.

[4]   C.J. Sung, H.J. Curran, Prog. Energy Combust. Sci. 44 (2014) 1–18.

[5]   C.G. Fotache, T.G. Kreutz, D.L. Zhu, C.K. Law, Combust. Sci. Technol. 109 (1995) 373–393.

[6]   T.G. Kreutz, M. Nishioka, C.K. Law, Combust. Flame 99 (1994) 758–766.

[7]   T.G. Kreutz, C.K. Law, Combust. Flame 104 (1996) 157–175.

[8]   C.G. Fotache, T.G. Kreutz, C.K. Law, Combust. Flame 108 (1997) 442–470.

[9]   C.G. Fotache, H. Wang, C.K. Law, Combust. Flame 117 (1999) 777–794.

[10]   C.G. Fotache, Y. Tan, C.J. Sung, C.K. Law, Combust. Flame 120 (2000) 417–426.

[11]   G. Jomaas, X.L. Zheng, D.L. Zhu, C.K. Law, Proc. Combust. Inst. 30 (2005) 193–200.

[12]   X.L. Zheng, T.F. Lu, C.K. Law, Proc. Combust. Inst. 31 (2007) 367–375.

[13]   W. Liu, A.P. Kelley, C.K. Law, Combust. Flame 157 (2010) 1027–1036.

[14]   J.D. Blouch, C.K. Law, Proc. Combust. Inst. 28 (2000) 1679–1686.

[15]   X.L. Zheng, T.F. Lu, C.K. Law, C.K Westbrook, H.J. Curran, Proc. Combust. Inst. 30 (2005) 1101–1109.

[16]   A.T. Holley, Y. Dong, M.G. Andac, F.N. Egolfopoulos, T. Edwards, Proc. Combust. Inst. 31 (2007) 1205–1213.

[17]   N. Liu, C. Ji, F.N. Egolfopoulos, Proc. Combust. Inst. 34 (2013) 873–880.

[18]   N. Liu, S. Mani Sarathy, C.K. Westbrook, F.N. Egolfopoulos, Proc. Combust. Inst. 34 (2013) 903–910.

[19]   N. Liu, C. Ji, F.N. Egolfopoulos, Combust. Flame 159 (2012) 465–475.

[20]   R. Seiser, K. Seshadri, E. Piskernik, A. Liñán, Combust. Flame 122 (2000) 339–349.

[21]   S. Humer, R. Seiser, K. Seshadri, Proc. Combust. Inst. 29 (2002) 1597–1604.

[22]   S. Humer, A. Frassoldati, S. Granata, T. Faravelli, E. Ranzi, R. Seiser, K. Seshadri, Proc. Combust. Inst. 31 (2007) 393–400.

[23] T. Bieleveld, A. Frassoldati, A. Cuoci, T. Faravelli, E. Ranzi, U. Niemann, K. Seshadri, Proc. Combust. Inst. 32 (2009) 493–500.

[24] R. Seiser, U. Niemann, K. Seshadri, Proc. Combust. Inst. 33 (2011) 1045–1052.

[25] R. Seiser, H. Pitsch, K. Seshadri, W.J. Pitz, H.J. Curran, Proc. Combust. Inst. 28 (2000) 2029–2037.

[26] G. Jomaas, X.L. Zheng, D.L. Zhu, C.K. Law, Proc. Combust. Inst. 30 (2005) 193–200.

[27] X.L. Zheng, C.K. Law, Combust. Flame 136 (2004) 168–179.

[28] X.L. Zheng, J.D. Blouch, D.L. Zhu, T.G. Kreutz, C.K. Law, Proc. Combust. Inst. 29 (2002) 1637–1643.

[29] W. Liu, D.L. Zhu, N. Wu, C.K. Law, Combust. Flame 157 (2010) 259–266.

[30] W. Liu, J.A. Koch, C.K. Law, Combust. Flame 158 (2011) 2145–2148.

[31] W. Liu, A.P. Kelley, C.K. Law, Proc. Combust. Inst. 33 (2011) 995–1002.

[32] K. Seshadri, S. Humer, R. Seiser, Combust. Theory Model. 12 (2008) 831–855.

[33] X. Gu, Z. Huang, S. Wu, Q. Li, Combust. Flame 157 (2010) 2318–2325.

[34] F. Wu, C.K. Law, Combust. Flame 160 (2013) 2744–2756.

[35] S.M. Sarathy, M.J. Thomson, C. Togbé, P. Dagaut, F. Halter, C. Mounaim-Rousselle, Combust. Flame 156 (2009) 852–864.

[36] C.M. Mitsingas, D.C. Kyritsis, J. Energy Eng. 140 (2014) A4014006.

[37] M.R. Harper, K.M. Van Geem, S.P. Pyl, G.B. Marin, W.H. Green, Combust. Flame 158 (2011) 16–41.

[38] J.K. Lefkowitz, J.S. Heyne, S.H. Won, S. Dooley, H.H. Kim, F.M. Haas, S. Jahangirian, F.L. Dryer, Y. Ju, Combust. Flame 159 (2012) 968–978.

[39] R. Grana, A. Frassoldati, T. Faravelli, U. Niemann, E. Ranzi, R. Seiser, R. Cattolica, K. Seshadri, Combust. Flame 157 (2010) 2137–2154.

[40] P. Dagaut, S.M. Sarathy, M.J. Thomson, Proc. Combust. Inst. 32 (2009) 229–237.

[41] D.M.A. Karwat, S.W. Wagnon, P.D. Teini, M.S. Wooldridge, J. Phys. Chem. A 115 (2011) 4909–4921.

[42] B.W. Weber, C.J. Sung, Energy & Fuels 27 (2013) 1688–1698.

[43] I. Stranic, D.P. Chase, J.T. Harmon, S. Yang, D.F. Davidson, R.K. Hanson, Combust. Flame 159 (2012) 516–527.

[44] G. Black, H.J. Curran, S. Pichon, J.M. Simmie, V. Zhukov, Combust. Flame 157 (2010) 363–373.

[45] A. Frassoldati, R. Grana, T. Faravelli, E. Ranzi, P. Oßwald, K. Kohse-Höinghaus, Combust. Flame 159 (2012) 2295–2311.

[46] S.S. Merchant, E.F. Zanoelo, R.L. Speth, M.R. Harper, K.M. Van Geem, W.H. Green, Combust. Flame 160 (2013) 1907–1929.

[47] K.M. Van Geem, S.P. Pyl, G.B. Marin, M.R. Harper, W.H. Green, Ind. Eng. Chem. Res. 49 (2010) 10399–10420.

[48] S.M. Sarathy, S. Vranckx, K. Yasunaga, M. Mehl, P. Oßwald, W.K. Metcalfe, C.K. Westbrook, W.J. Pitz, K. Kohse-Höinghaus, R.X. Fernandes, H.J. Curran, Combust. Flame 159 (2012) 2028–2055.

[49] P.S. Veloo, Y.L. Wang, F.N. Egolfopoulos, C.K. Westbrook, Combust. Flame 157 (2010) 1989–2004.

[50] J. Hashimoto, K. Tanoue, N. Taide, Y. Nouno, Proc. Combust. Inst. (2014) doi: 10.1016/j.proci.2014.05.013.

[51] C.L. Yaws, Yaws' Handbook of Thermodynamic and Physical Properties of Chemical Compounds, Knovel, 2003.

[52] C.J. Sung, J.S. Kistler, M. Nishioka, C.K. Law, Combust. Flame 105 (1996) 189–201.

[53] K. Seshadri, F.A. Williams, Int. J. Heat Mass Transf. 21 (1978) 251–253.

[54] M.D. Smooke, I.K. Puri, K. Seshadri, Symp. Combust. 21 (1988) 1783–1792.

[55] M. Nishioka, C.K. Law, T. Takeno, Combust. Flame 104 (1996) 328–342.

[56] C.J. Sung, J.B. Liu, C.K. Law, Combust. Flame 102 (1995) 481–492.

[57] K.E. Niemeyer, C.J. Sung, M.P. Raju, Combust. Flame 157 (2010) 1760–1770.

[58] K.E. Niemeyer, C.J. Sung, Combust. Flame 158 (2011) 1439–1443.

[59] K.E. Niemeyer, C.J. Sung, Combust. Flame 161 (2014) 2752–2764.

[60] K.E. Niemeyer, C.J. Sung, Energy & Fuels 29 (2015) 1172–1185.

[61] L. Tosatto, B. La Mantia, H. Bufferand, P. Duchaine, A. Gomez, Proc. Combust. Inst. 32 (2009) 1319–1326.

[62] F. Carbone, A. Gomez, Combust. Flame 161 (2014) 453–464.

[63] M. Yamamoto, S. Duan, S. Senkan, Combust. Flame 151 (2007) 532–541.
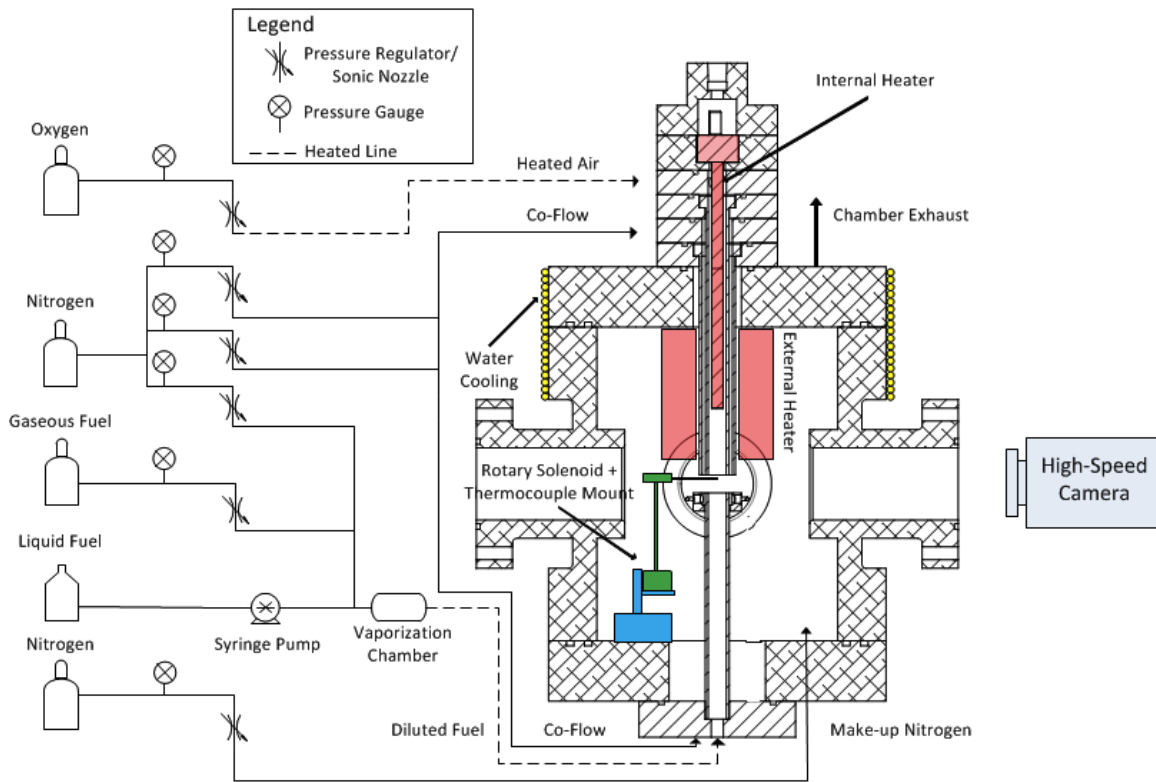
Figure 1: Diagram of the flow control, heating, and measurement systems for the counterflow ignition apparatus.
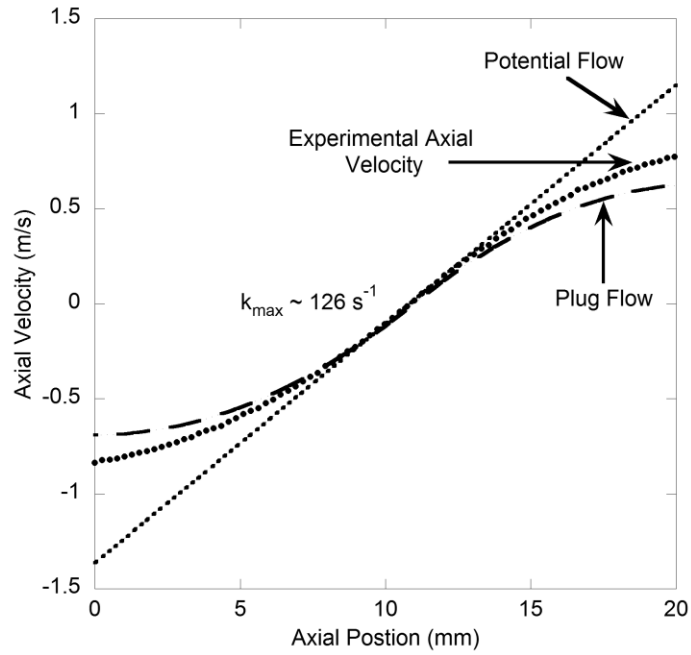
Figure 2: Comparison of experimentally measured axial velocities to plug- and potential-flow models under unheated, P = 1 atm, $k' = 150$ s^{-1} conditions.
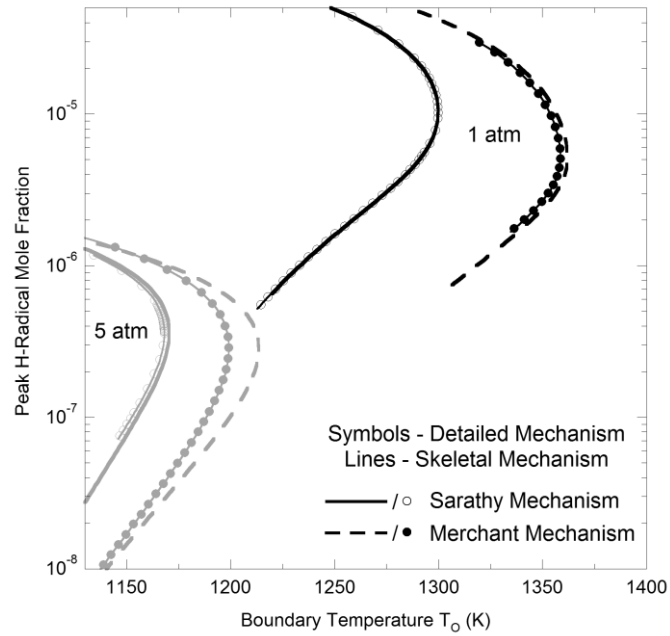
Figure 3: Comparison of computed ignition response curves between the detailed and skeletal mechanisms of Sarathy et al. [48] and Merchant et al. [46] for *n*-butanol at 1 atm, $k' = 300$ s^{-1} and 5 atm, $k' = 500$ s^{-1}.
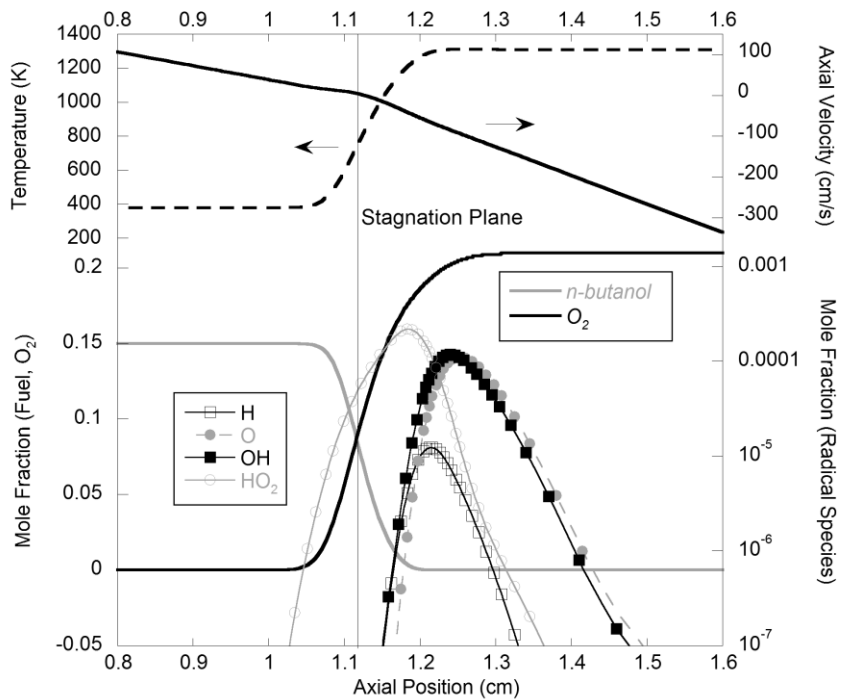
Figure 4: Typical thermal mixing zone/ignition kernel structure at 1 atm, $k' = 350$ s^{-1}, $X_f = 0.15$, computed using the skeletal *n*-butanol mechanism derived from Sarathy et al. [48] and evaluated at the ignition turning point.
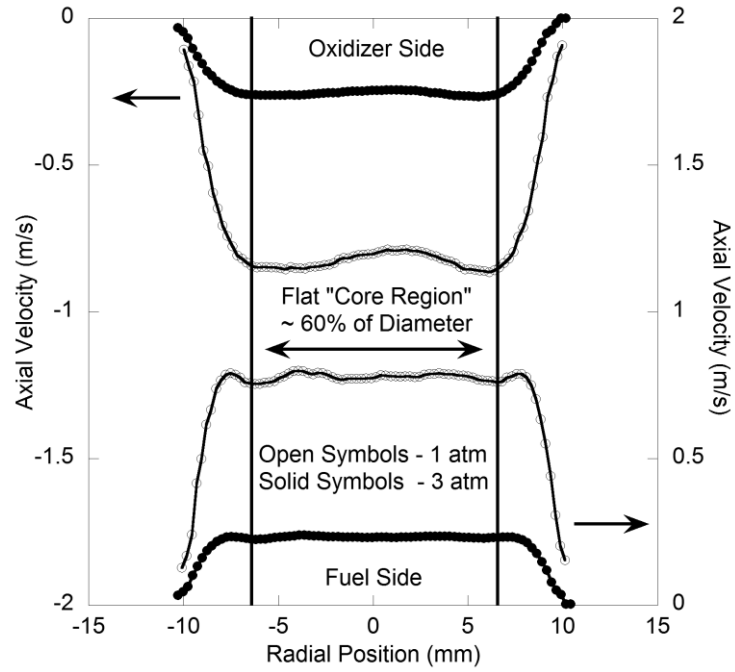
Figure 5: Axial velocity as a function of radial distance from the experimental centerline at *k'* = 150 s^{-1}, 1 and 3 atm, measured at 1 mm axial distances from air and fuel duct exits. Results are obtained for room temperature flows.
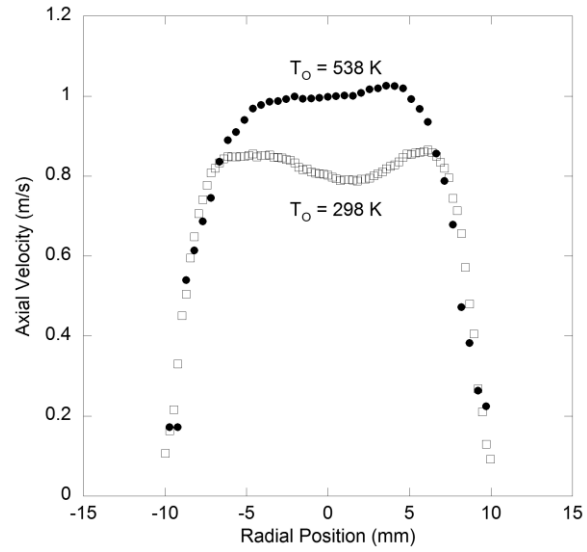
Figure 6: Comparison between air duct axial velocity profiles across the air duct radius for unheated and slightly heated cases at 1 atm using identical mass flow rates to those used in Fig. 5.
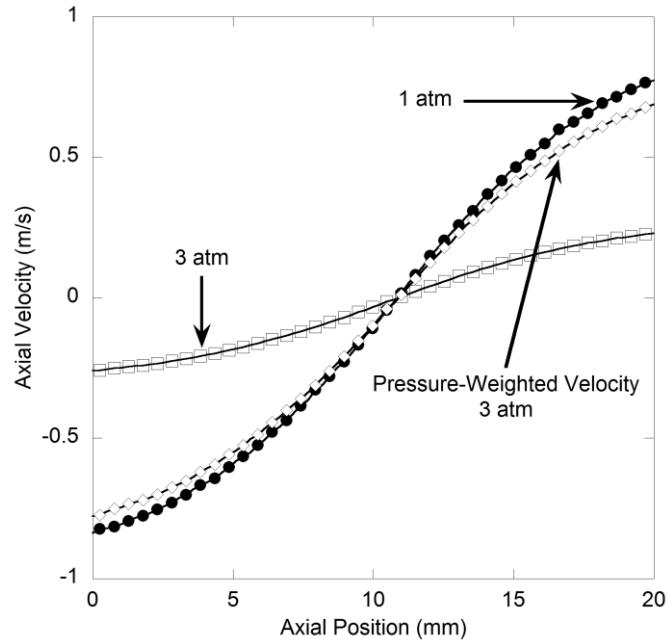
Figure 7: Axial velocity profiles (raw and pressure-weighted) along the experimental centerline for P = 1, 3 atm, $k' = 150$ s^{-1}.
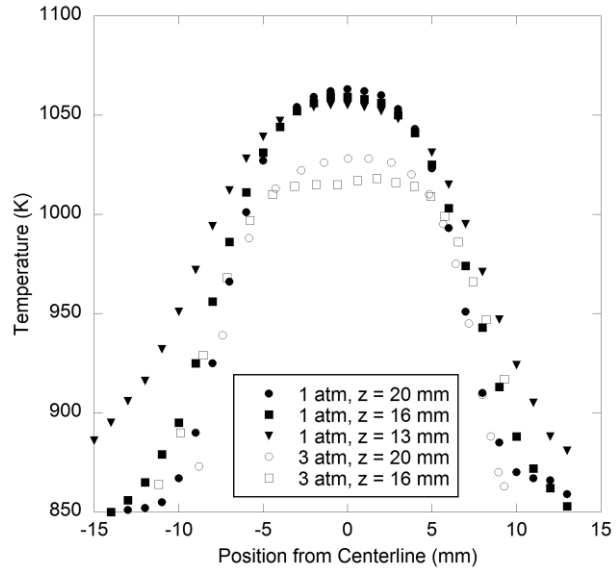
Figure 8: Uncorrected radial temperature profiles at $k' = 300$ s^{-1} for 1 and 3 atm and a centrally-located stagnation plane. Open symbols represent 3 atm chamber pressure, while filled symbols represent 1 atm pressure. Oxidizer duct exit is located at z=20 mm.
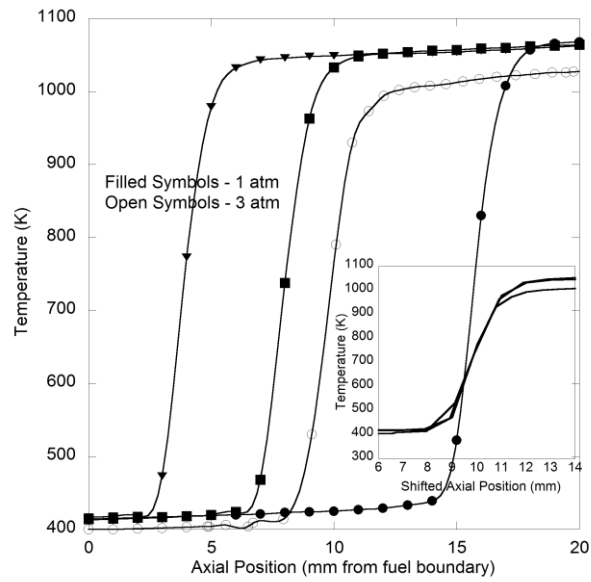
Figure 9: Uncorrected axial temperature profiles at 1 and 3 atm, $k' = 300$ s^{-1} and constant heater power. Various stagnation plane locations corresponding to varied oxidizer-side mass flow rates are shown for 1 atm. Inset: position-shifted temperature profiles demonstrate the similarity in the axial temperature profile for a constant pressure-weighted strain rate.
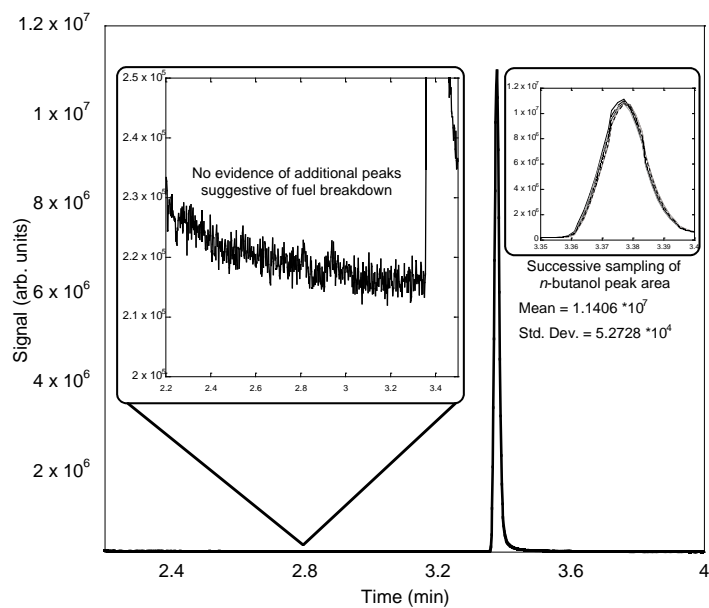
Figure 10: GC/MS results for $X_f = 0.15$ at 1 atm. Main graph: typical peak for *n*-butanol. Peak area shows agreement within 11% of expected peak area. Left inset: expanded y-axis showing a lack of additional peaks, and hence indicating no fuel breakdown. Right inset: representative measurements from successive sampling, demonstrating repeatability of flow system and sampling procedure.
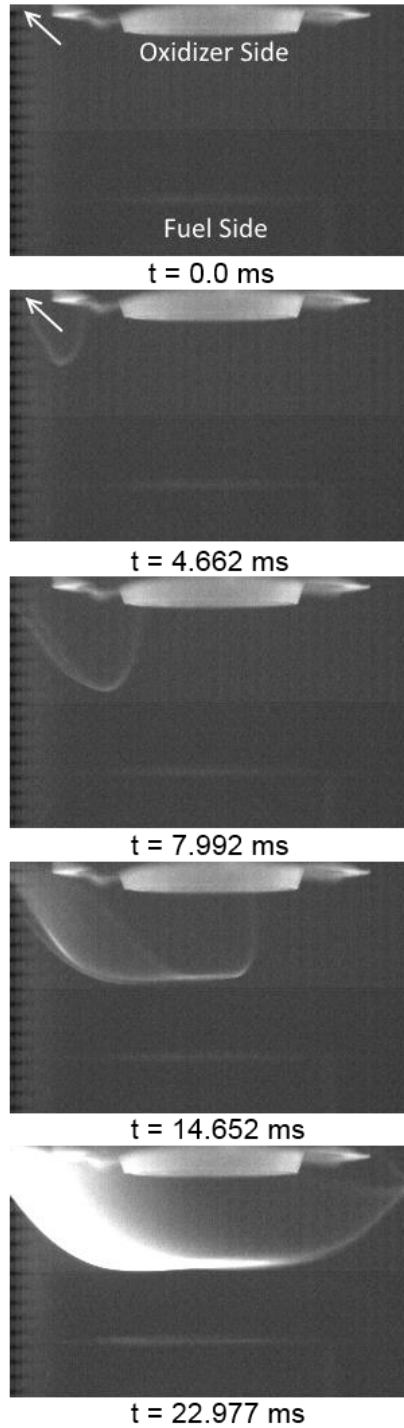
Figure 11: Example of an out-of-bounds ignition event at 4 atm, k'=350 s^{-1}, and X$_f$ = 0.15 fuel

loading. Arrow indicates the location where the flame enters frame (not readily visible at t = 0.0

ms).
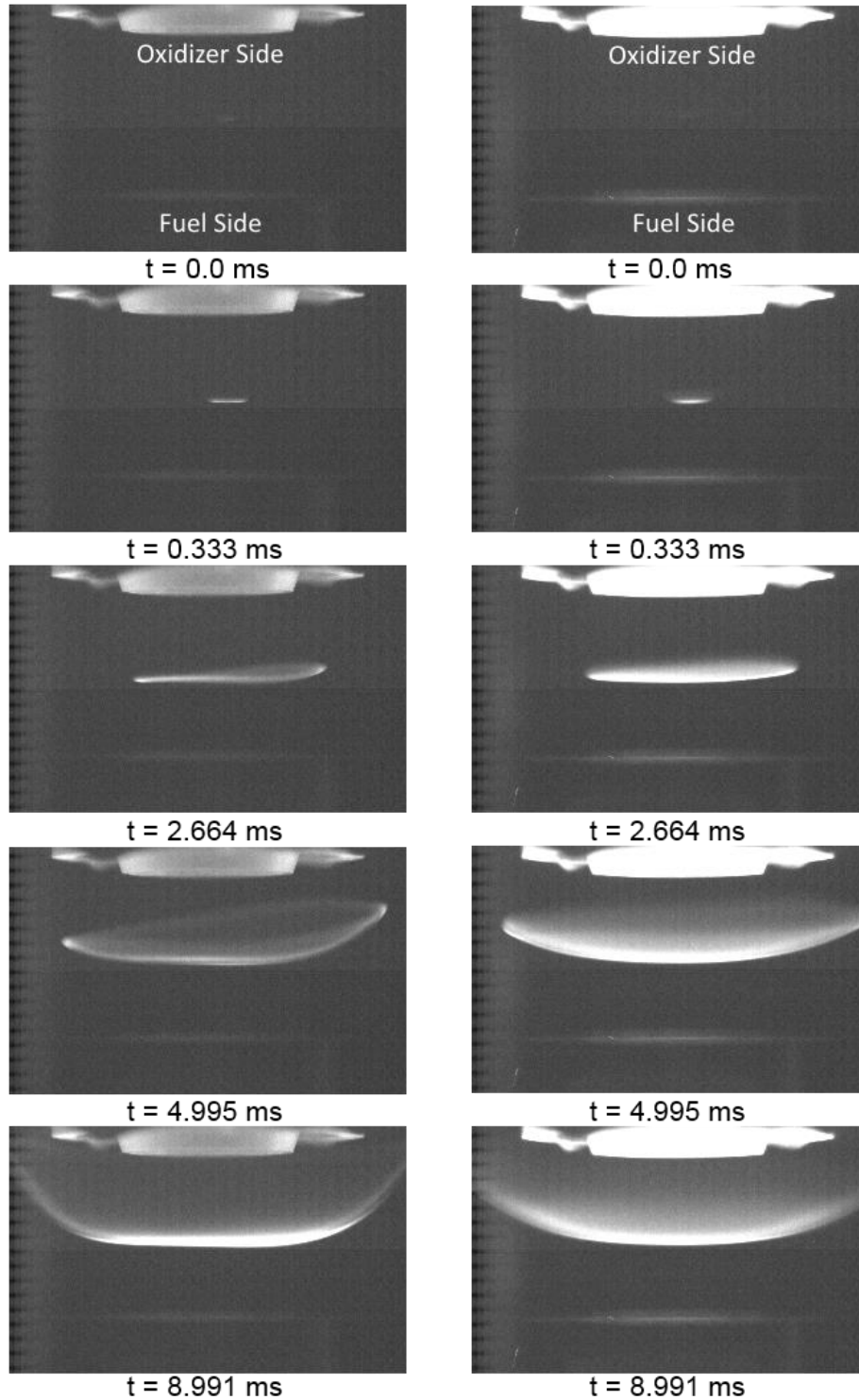
Figure 12: High-speed imagery of the ignition event using *n*-butanol at $k' = 350$ s^{-1} and $X_f = 0.15$ fuel loading, for 1 atm (left) and 3 atm (right) chamber pressures. The slight asymmetry observed in the third and fourth frames of the 3 atm history are the result of slightly off-centerline ignition, both left-to-right and front-to-back.
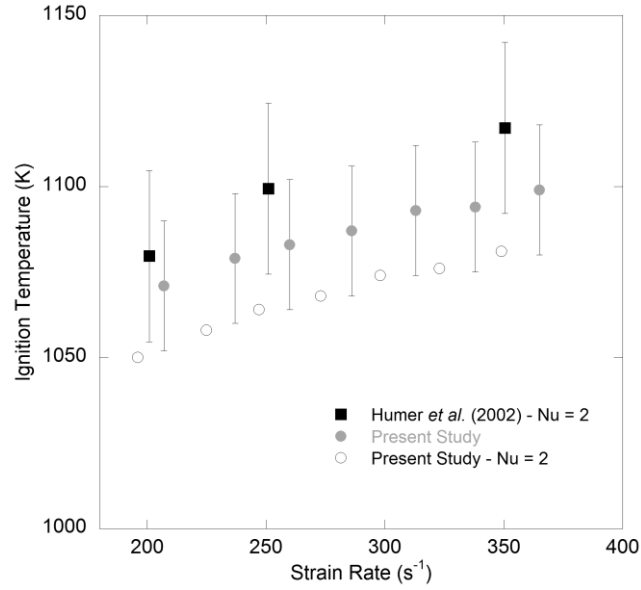
Figure 13: Comparison between the ethylene ignition results from Humer et al. [21] and the present study. Ignition temperatures from the present study are given using the radiation correction method presented in the Supplementary Material, as well as using the constant Nu = 2 assumption in keeping with the methodology of Humer et al. [21]. Error bars represent estimates of total uncertainty.
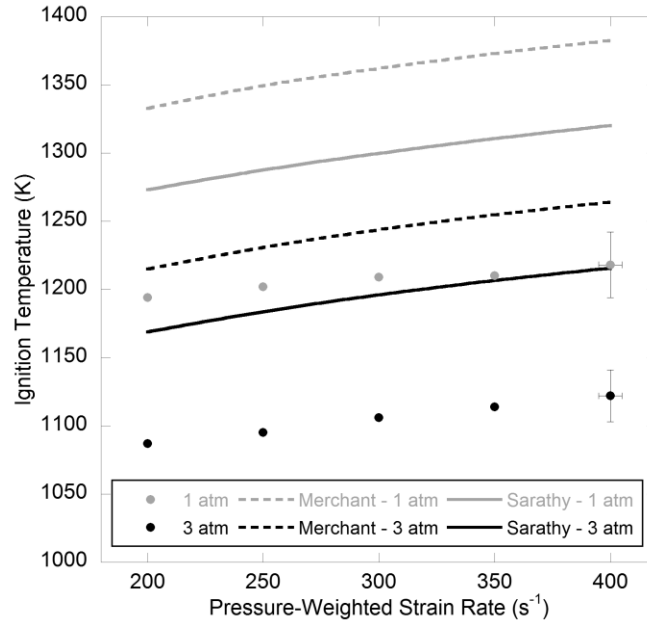
Figure 14: Ignition temperatures of *n*-butanol ($X_f = 0.15$) as a function of pressure-weighted strain rate at 1 and 3 atm, compared to the numerical simulation results predicted by the skeletal mechanisms derived from Merchant et al. [46] and Sarathy et al. [48]. Error bars represent total estimated uncertainty.
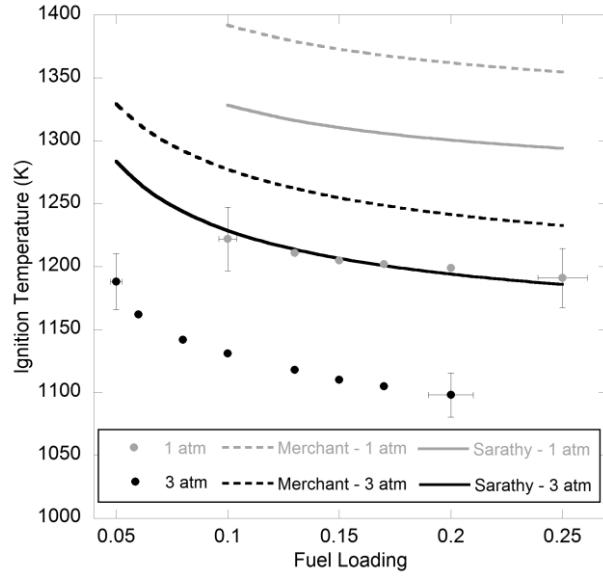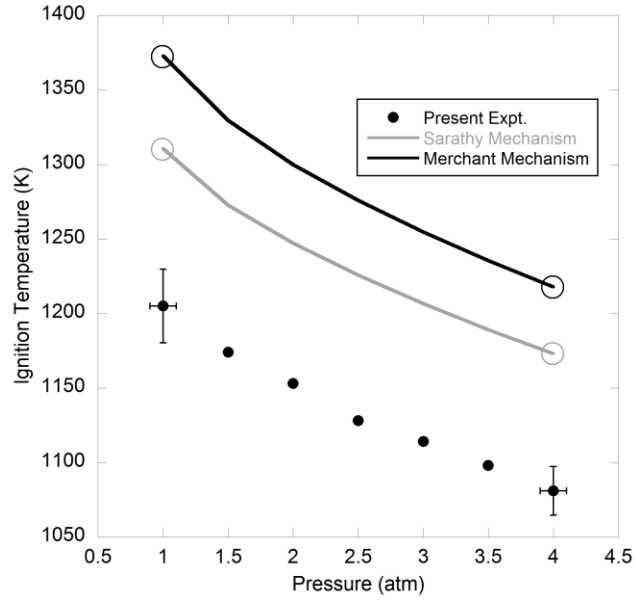
Figure 15: Ignition temperatures of *n*-butanol as a function of fuel loading at 1 and 3 atm and *k'* = 350 s^{-1}, compared to the results predicted by the skeletal mechanisms derived from Merchant et al. [46] and Sarathy et al. [48]. Error bars represent total estimated uncertainty.

Figure 16: Ignition temperatures of *n*-butanol as a function of pressure at $k' = 350$ s^{-1} and $X_f = 0.15$, compared to the results predicted by the skeletal mechanisms derived from Merchant et al. [46] and Sarathy et al. [48]. Error bars represent total estimated uncertainty. Circles represent the data points at which the sensitivity analysis of Fig. 17 is conducted.
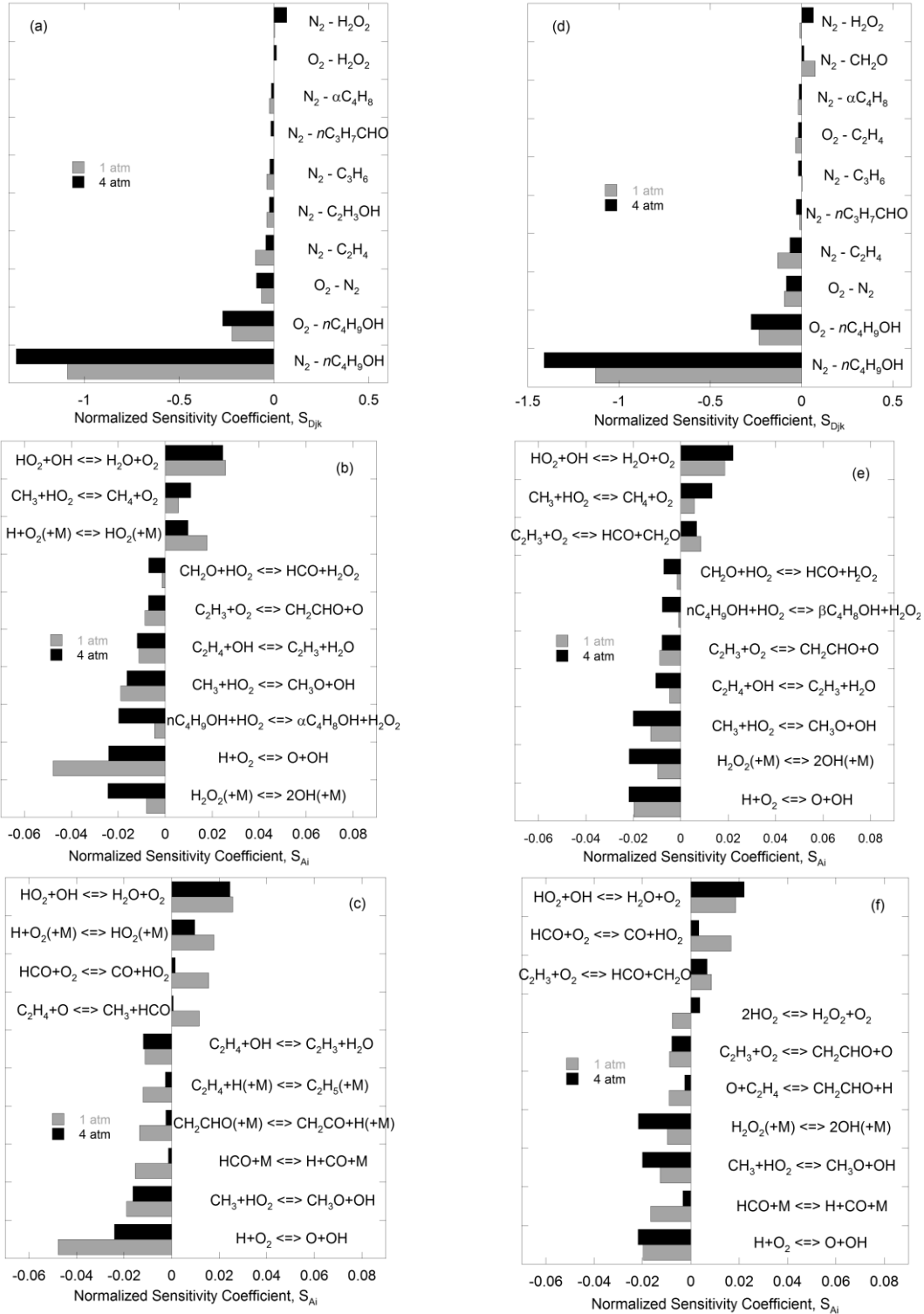
Figure 17: Sensitivity analyses at 1 and 4 atm, $k' = 350$ s^{-1}, $X_f = 0.15$ using the Sarathy mechanism (a-c) and Merchant mechanism (d-f). (a/d): Sensitivity to binary diffusion coefficients. (b/e): Sensitivity to reaction rates, sorted by largest magnitude at 4 atm. (c/f): Sensitivity to reaction rates, sorted by largest magnitude at 1 atm.
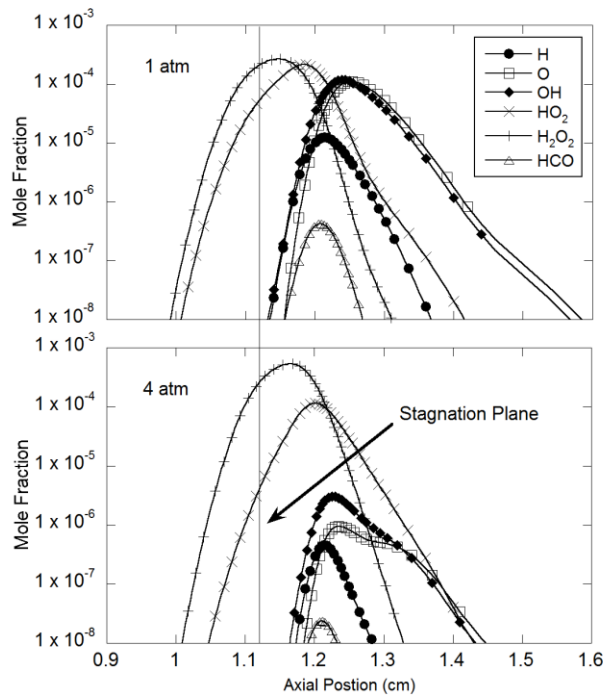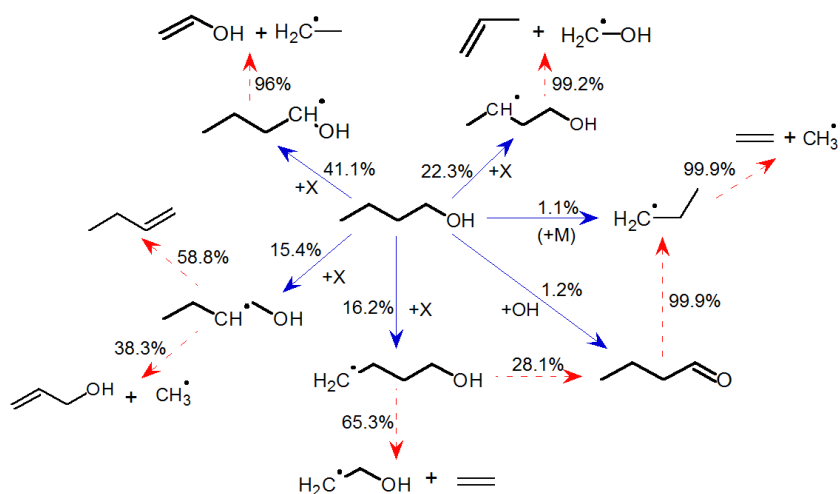
Figure 18: Important species spatial profiles based on the Sarathy mechanism compared between 1 and 4 atm at $k' = 350$ s^{-1} and $X_f = 0.15$.

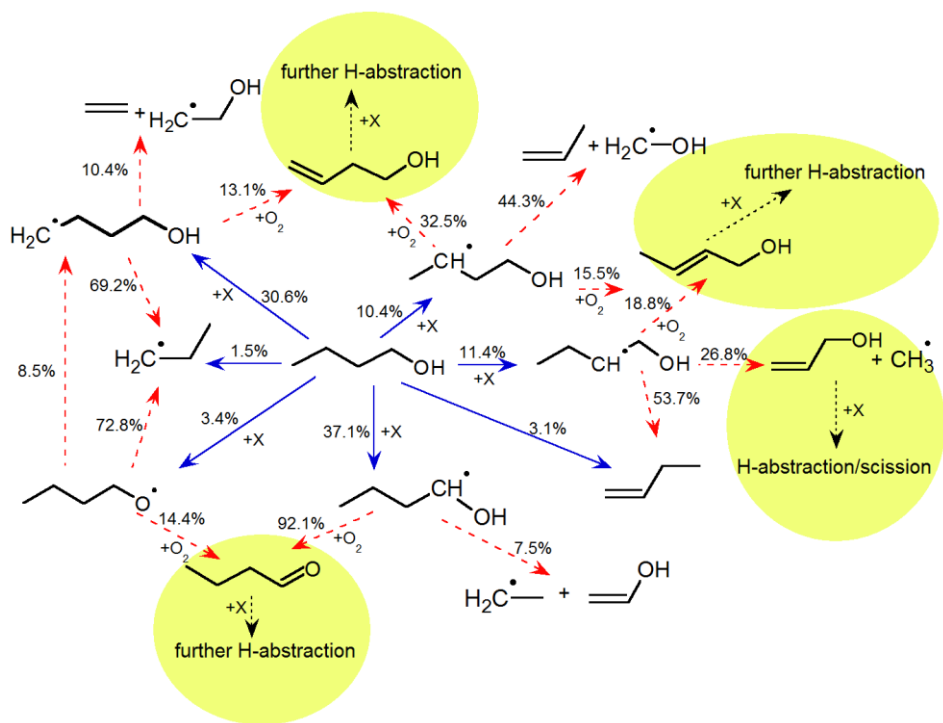Figure 19: Integrated path flux analysis maps computed at 1 atm, $k' = 350$ s^{-1}, and $X_f = 0.15$, demonstrating the differing chemical pathways predicted by the Merchant [46] and Sarathy [48] mechanisms at their respective turning points. a) Sarathy mechanism, evaluated at T_{ig}=1310 K, and b) Merchant mechanism, evaluated at T_{ig}=1372 K, with highlighted areas indicating pathways that significantly differ from those predicted by the Sarathy mechanism. "X" denotes a radical species, and a lack of a modifier denotes a unimolecular reaction.